Formation of the postmitotic nuclear envelope from extended ER cisternae precedes nuclear pore assembly

Lei Lu,[1,2,3] Mark S. Ladinsky,[4,5] and Tomas Kirchhausen[1,2]

[1]Department of Cell Biology, Harvard Medical School, Boston, MA 02115
[2]Immune Disease Institute and Program in Cellular and Molecular Medicine, Children's Hospital Boston, Boston, MA 02115
[3]School of Biological Sciences, Nanyang Technological University, Singapore 639798
[4]Division of Biology and [5]Howard Hughes Medical Institute, California Institute of Technology, Pasadena, CA 91125

During mitosis, the nuclear envelope merges with the endoplasmic reticulum (ER), and nuclear pore complexes are disassembled. In a current model for reassembly after mitosis, the nuclear envelope forms by a reshaping of ER tubules. For the assembly of pores, two major models have been proposed. In the insertion model, nuclear pore complexes are embedded in the nuclear envelope after their formation. In the prepore model, nucleoporins assemble on the chromatin as an intermediate nuclear pore complex before nuclear envelope formation. Using live-cell imaging and electron microscope tomography, we find that the mitotic assembly of the nuclear envelope primarily originates from ER cisternae. Moreover, the nuclear pore complexes assemble only on the already formed nuclear envelope. Indeed, all the chromatin-associated Nup107–160 complexes are in single units instead of assembled prepores. We therefore propose that the postmitotic nuclear envelope assembles directly from ER cisternae followed by membrane-dependent insertion of nuclear pore complexes.

Introduction

The nuclear envelope is a specialized, double-membrane domain of the ER that encloses the chromatin and separates it from the cytoplasm (Baumann and Walz, 2001; Burke and Ellenberg, 2002). The two membranes of the nuclear envelope join with each other around the nuclear pores, structures that allow transport of macromolecules between the cytosol and the nucleus (Hetzer et al., 2005). A nuclear pore forms by assembly of the ∼120-MD nuclear pore complex, which in mammals comprises >30 proteins known as nucleoporins or Nups. The nuclear envelope and pores disassemble at the end of prophase. The transmembrane proteins of the nuclear envelope move into the mitotic ER, and the soluble components of the nuclear pore complex disperse in the cytosol (Ellenberg et al., 1997; Yang et al., 1997). Reassembly of the nuclear envelope and nuclear pore complexes occurs at the end of mitosis, and further doubling of the number of pores occurs during interphase (D'Angelo et al., 2006).

It has been proposed that the postmitotic nuclear envelope arises by the fusion of mitotic ER tubules as they attach to the surface of the chromosome mass followed by lateral expansion around the chromatin. In support of this model, there are data from in vitro fluorescence microscopy demonstrating nuclear envelope reconstitution from a *Xenopus laevis* extract enriched in the tubular ER network (Anderson and Hetzer, 2007) and in vivo images of U2OS cells showing the presence of a few ER tubules next to the chromosomes during anaphase (Anderson and Hetzer, 2008). We have found, however, that during mitosis, the ER of mammalian cells undergoes a massive reorganization, from the mix of tubules and cisternae normally present during interphase to extended cisternae. The extended cisternae remain from the end of prophase through the end of mitosis, returning to a mixture of tubules and cisternae after cytokinesis. These observations were made by rapid, live-cell 3D imaging with confirmation from high-resolution electron tomography of samples preserved by high-pressure freezing and freeze substitution

Correspondence to Tomas Kirchhausen: kirchhausen@crystal.harvard.edu; or Lei Lu: lulei@ntu.edu.sg

Abbreviations used in this paper: ELYS, embryonic large molecule derived from yolk sac; IBB, importin-β binding domain.

The Rockefeller University Press $30.00
J. Cell Biol. Vol. 194 No. 3 425–440
www.jcb.org/cgi/doi/10.1083/jcb.201012063

(Lu et al., 2009). Our findings prompted us to readdress the question of mitotic nuclear envelope assembly using the same sensitive imaging approaches. Here, we show that nuclear envelope reformation occurs primarily by coordinated direct contact of mitotic ER cisternae with the chromosome mass. In HeLa cells, nuclear envelope formation starts at the radial periphery of the two disk-shaped chromosome masses, called here the "rim," and continues with a growing phase characterized by centripetal expansion of the nascent nuclear envelope along the chromosome masses and ending with complete enclosure.

A second question we address here concerns when and where nuclear pore complex formation initiates during cell division. According to the insertion model of nuclear pore formation, presence of the nuclear envelope is required for the stepwise assembly of the nuclear pore (Macaulay and Forbes, 1996; Goldberg et al., 1997; Kiseleva et al., 2001). In contrast, the prepore model proposes that the first event is the recruitment to the chromosome mass of nucleoporin complexes, for example Nup107–160, which then associate into higher order substructures on regions devoid of a nuclear envelope; these complexes then recruit the remaining nucleoporins after the nuclear envelope forms (Comings and Okada, 1970; Maul, 1977; Sheehan et al., 1988; Bodoor et al., 1999; Walther et al., 2003; Antonin et al., 2005; Dultz et al., 2008; Dultz and Ellenberg, 2010).

By using sensitive, high-resolution live-cell imaging methods, we have established a temporal sequence of events, in which formation of nuclear envelope membranes is an absolute requirement for successful postmitotic assembly of nuclear pores. By a single molecule approach developed for this study, we find that all the chromatin-associated Nup107–160 complexes are in single units instead of assembled prepores. The assembly of soluble Nup107–160 complexes into higher order structures occurs only at sites on the chromatin surface that are already covered with the nuclear envelope. Recruitment of Nup107–160 complexes is followed by local assembly of the remaining nuclear pore components, ending with the formation of functional pores. These new in vivo data support an insertion model for postmitotic nuclear pore complex assembly.

Results

Extended ER cisternae generate the postmitotic nuclear envelope membrane

We showed previously that the mitotic ER is made primarily of extended cisternae that on single confocal optical sections display characteristically curvilinear profiles (Lu et al., 2009). We also observed the merging of nuclear envelope transmembrane proteins with the ER in agreement with previous studies (Ellenberg et al., 1997; Yang et al., 1997). To investigate how the nuclear envelope reforms during mitosis, we acquired single optical sections by live-cell imaging using spinning-disk confocal microscopy. We determined the spatial and temporal characteristics of the nuclear envelope assembly in HeLa cells, in which ER membranes and chromatin had been fluorescently tagged with GFP-Sec61β and histone2B-mCherry (H2B-mCherry), respectively. The onset of anaphase was defined by the time at which the daughter chromosomes started to separate from each other (Video 1); this step was followed by the collapse of each set of daughter chromosomes into a disk-shaped chromosome mass, onto which the nuclear envelope subsequently assembled (Fig. 1 A). To facilitate the analysis, we divided the surface of the disk-shaped chromosome mass into a rim region, a proximal side facing the spindle pole and a distal side facing the cell interior (Fig. 1 B). The nuclear envelope initiation step (Fig. 1 A, 0 s, arrows) was defined as the first observable tight association between ER cisternae and chromosome mass, which always occurred at the rim, typically 450 ± 60 s ($n = 5$) after onset of anaphase (Fig. S1), in agreement with earlier snapshot observations using fluorescent or electron microscopy (Chaudhary and Courvalin, 1993; Haraguchi et al., 2008). The ER membranes in close contact with the chromosome mass rapidly accumulated resident nuclear envelope membrane proteins, such as LBR (lamin B receptor), emerin, and sun2, concomitant with loss of the ER membrane protein reticulon4a, thus indicating a transition from the ER to the nascent nuclear envelope (Fig. 2 and Fig. S2). After a delay of 110 ± 50 s ($n = 5$), the nascent nuclear envelope began to extend along the proximal and distal sides of the chromosome mass (Fig. 1 A, 120–420 s) at a maximal rate of 1.3 ± 0.4 µm/min ($n = 5$). At 840 ± 110 s ($n = 5$) after onset of anaphase, the migrating fronts eventually met to seal up all the visible gaps (Fig. 1 A, 480 s; and Fig. S1 B), thus defining the completion of nuclear envelope formation. The period between nuclear envelope initiation and completion was 410 ± 60 s ($n = 10$). Just as in HeLa cells, nuclear envelope assembly in 293 cells originated from extended ER cisternae and began along the rim of the chromosome mass followed by centripetal growth along both sides of the chromosome mass (unpublished data). In contrast, nuclear envelope assembly in BSC1 cells initiated not only at the rim but also at multiple sites on the proximal and distal sides of the chromosome mass (Video 2).

We expanded the 2D live-cell imaging to observations using dual-color 3D time-lapse imaging combined with surface rendering of GFP-Sec61β and H2B-mCherry in mitotic HeLa cells (Fig. 1 B). These experiments confirmed that the nuclear envelope forms from the deposition of ER cisternae to the rim of the disk-shaped chromosome mass, with growth extending toward the spindle axis. We believe that the asymmetric nuclear envelope assembly is related to the presence of the spindle microtubules, which hinder the access of the extended ER cisternae to the distal and proximal sides along the opposite sides of the chromosome mass. As shown in Fig. 3 A, the ER is excluded from the spindle pole and the space between the two chromosome masses, both of which are occupied by spindle microtubules as demonstrated previously (Haraguchi et al., 2008). Access of ER cisternae to the proximal and distal sides of the chromosome mass can be accelerated by nocodazole-mediated depolymerization of spindle microtubules (Fig. 3, compare A with B; and compare Video 3 with Video 4), leading to simultaneous nuclear envelope formation at multiple sites at the rim, the proximal and distal sides of the chromosome mass, and hence, accelerated completion from 410 ± 60 s ($n = 10$) in control cells to 340 ± 50 s ($n = 3$) in nocodazole-treated cells. Conversely, interference with dissolution of the spindle should retard nuclear envelope assembly, and stabilization of the spindle microtubules

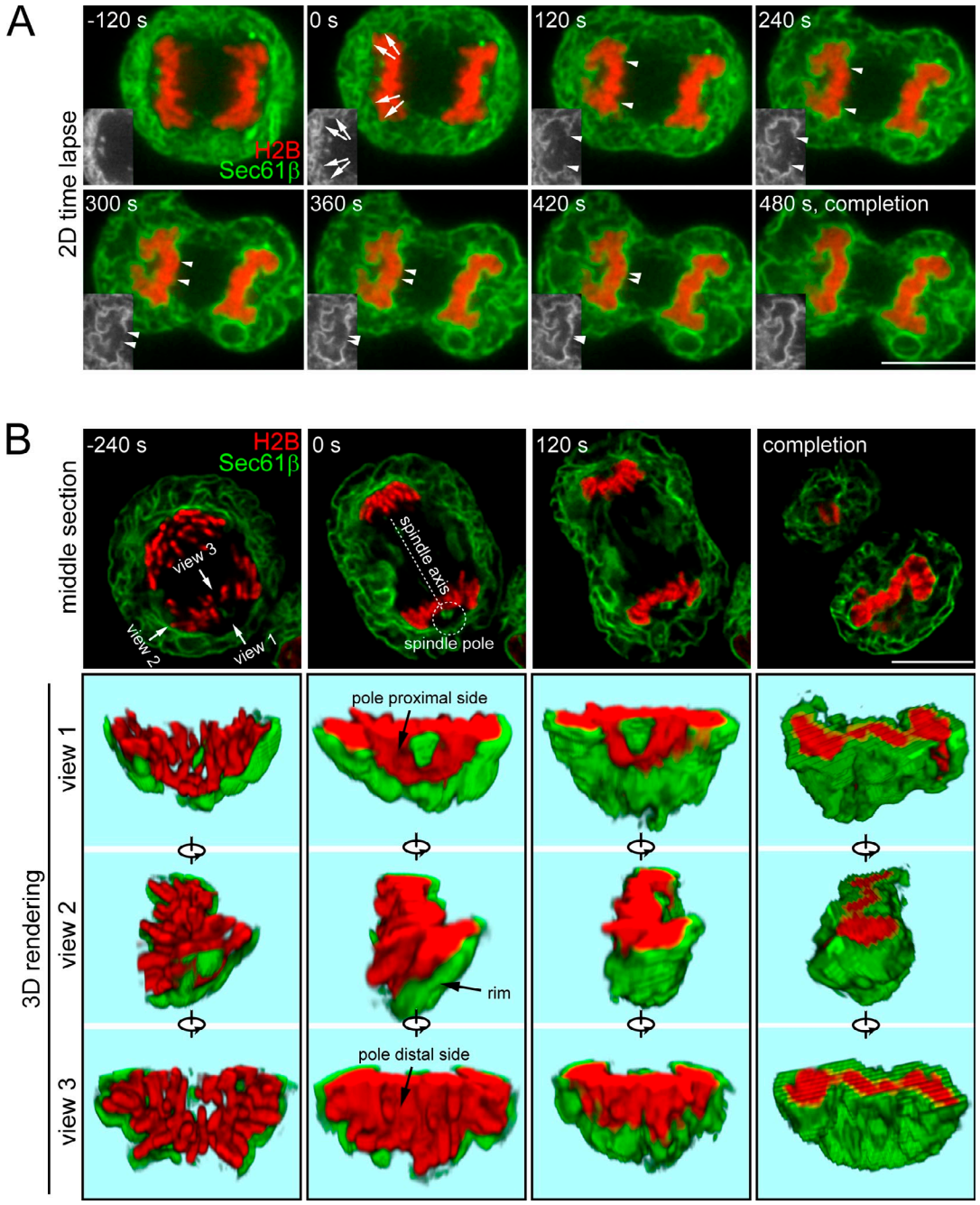

Figure 1. **Mitotic assembly of the nuclear envelope on the chromosome mass.** Live-cell images were acquired from mitotic HeLa cells expressing GFP-Sec61β and H2B-mCherry. (A) 2D time-lapse series showing formation of the nuclear envelope on the chromosome mass (also see Video 1). Arrows indicate the rim of the chromosome mass, at which ER cisternae make initial contacts (0 s). Arrowheads follow the migrating edge of the nascent nuclear envelope from the rim to the center of the chromosome mass (120–420 s). The monochrome images highlight the nuclear envelope. (B) Assembly of the nuclear envelope followed in 3D. Deconvolved images from a mitotic cell acquired at various time points in 3D. The top row shows 2D images from the middle section. The dotted line labeled spindle axis connects the two spindle poles. The columns below show 3D renderings of the right chromosome mass together with the associated nuclear envelope. For clarity, only the bottom half of the chromosome mass is shown. The three time points (−240 s, 0 s, and 120 s) are from the same anaphase cell. The 0-s time point corresponds approximately to the onset of nuclear envelope assembly. The image set labeled completion is from another cell that has just completed nuclear envelope assembly. Views 1–3 show three regions on the chromosome mass surface. View 1 shows spindle pole proximal side; View 2 shows the rim; View 3 shows the spindle pole distal side. Bars, 10 µm.

by taxol treatment during early anaphase indeed delayed nuclear envelope completion, increasing the total time to 1,200 ± 300 s (n = 3) in taxol-treated cells (Fig. 3 C and Video 5).

Our previous demonstration that the mitotic ER is made up of extended cisternae rather than tubules (Lu et al., 2009) leads to the prediction that the postmitotic nuclear envelope is formed directly from ER cisternae. Indeed, dual-color 3D live-cell imaging of HeLa cells expressing both Sec61β and H2B clearly shows continuity between the extended ER cisternae and the nascent nuclear envelope in contact with the chromosome

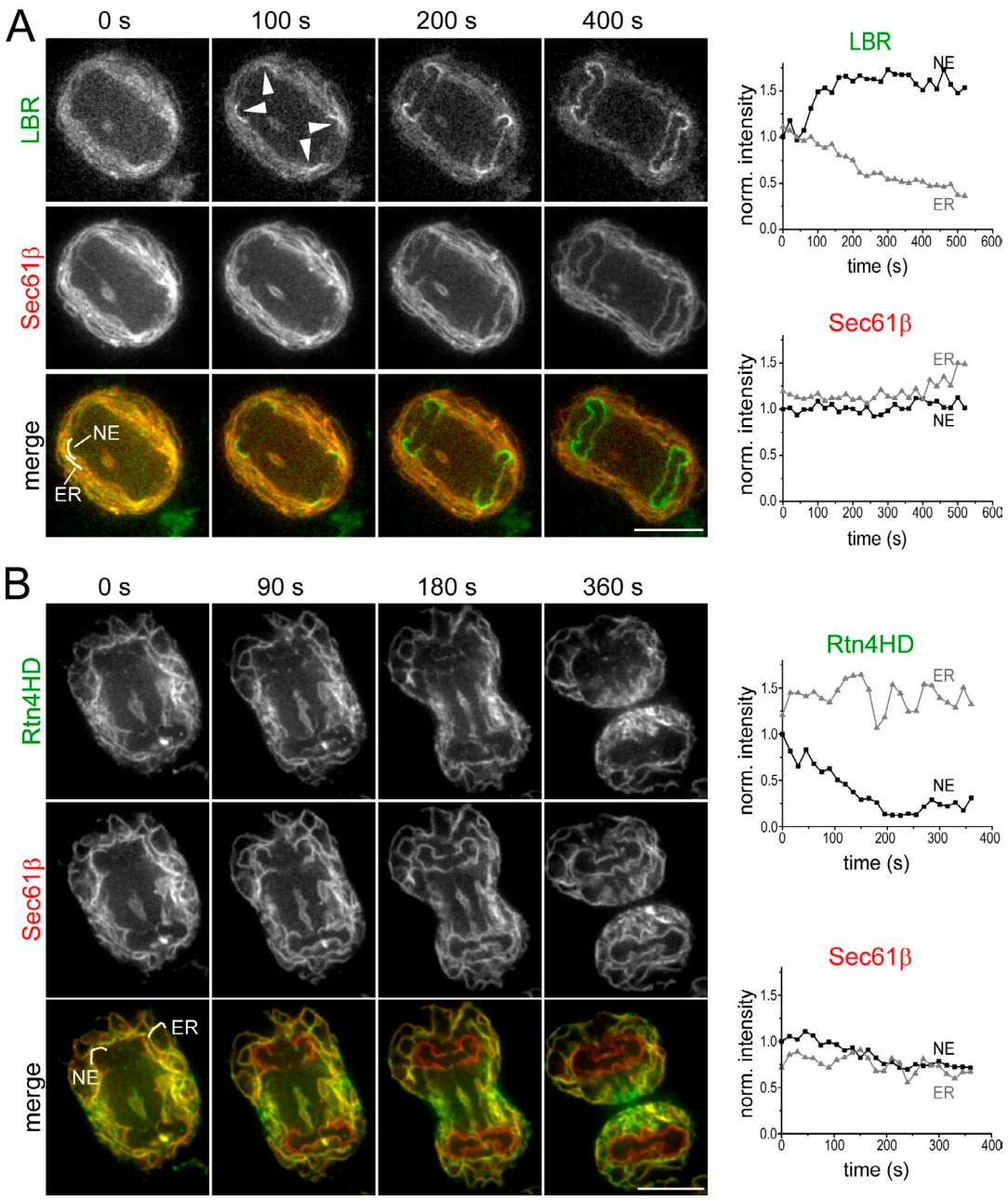

Figure 2. **Transition during mitosis from ER cisternae to the nuclear envelope.** (A and B) 2D time-lapse series from a mitotic HeLa cell expressing mCherry-Sec61β and LBR-GFP (A) or GFP-Rtn4HD (B) were acquired during mitotic nuclear envelope assembly. The tracings correspond to the normalized mean fluorescence intensity determined for Sec61β, LBR, and Rtn4HD in the masked regions representing peripheral ER and nascent nuclear envelope (NE). All data from A and B are representative results of three cells. norm., normalized. Bars, 10 µm.

mass (Fig. 4 A and Fig. S3 A). We obtained similar results with BSC1 cells (Fig. 4 B) even though nuclear envelope assembly initiates at multiple sites on the chromosome mass, suggesting that formation of the postmitotic nuclear envelope by the extended ER cisternae does not depend on where assembly begins.

High-resolution EM tomography of the nascent nuclear envelope

To validate the contribution of extended ER cisternae as a major membrane source for the postmitotic assembly of the nuclear envelope, we obtained high-resolution images of the nascent nuclear envelope using EM tomographic reconstruction of samples preserved by high-pressure freezing and freeze substitution. BSC1 cells completing metaphase were first identified at low magnification by the appearance of the cell shape and chromosomes (Fig. 4 C, a). In agreement with our previous observations (Lu et al., 2009), the vast majority of the mitotic ER was in extended cisternae, with a typical luminal spacing of ∼120 nm, dotted with ribosomes along both surfaces and with no indication of tubules. We could capture instances showing the ER in close contact with the chromosome mass, which we propose to be a nascent nuclear envelope. The example in Fig. 4 C illustrates such a case: a portion of an extended ER cisterna has

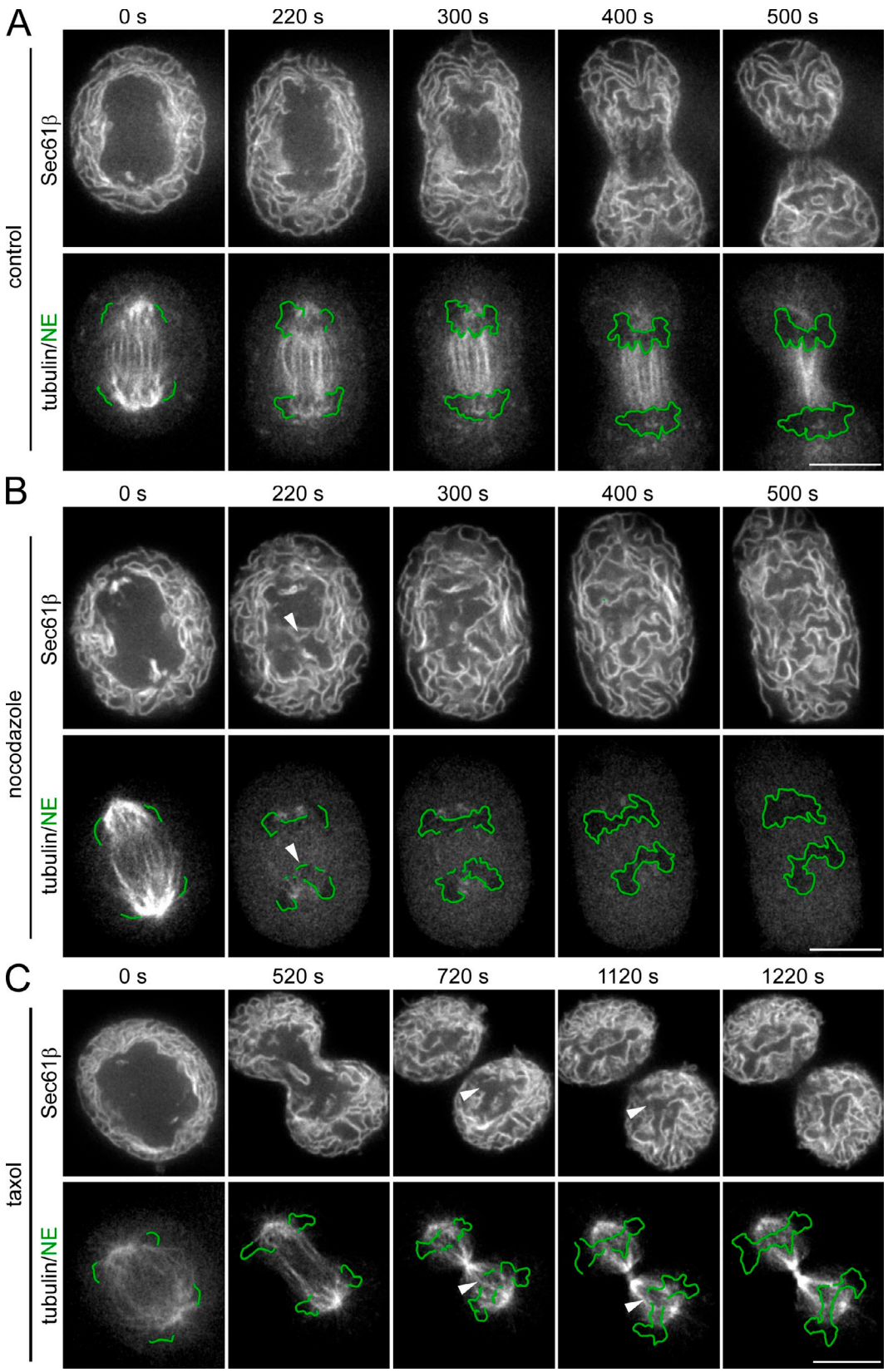

Figure 3. **Effect during mitosis of spindle microtubules on nuclear envelope formation.** 2D time-lapse images from mitotic HeLa cells expressing GFP-Sec61β and mCherry-tubulin were acquired during nuclear envelope assembly. (A) Control (also see Video 3) in the absence of nocodazole. (B) Nocodazole treated (also see Video 4). 33 µM nocodazole was added shortly after the onset of anaphase. Arrowheads indicate nuclear envelope initiation at the pole distal region of the chromosome mass. (C) Taxol treated (also see Video 5). 2 µM taxol was added shortly after the onset of anaphase. Arrowheads indicate a gap on the nuclear envelope obstructed by stabilized spindle microtubules. 0 s corresponds to the onset of nuclear envelope formation. Nuclear envelope (NE; green lines) corresponds to regions containing Sec61β on the contour of the chromosome mass, visible as a dark region because of its exclusion of soluble mCherry-tubulin. Bars, 10 µm.

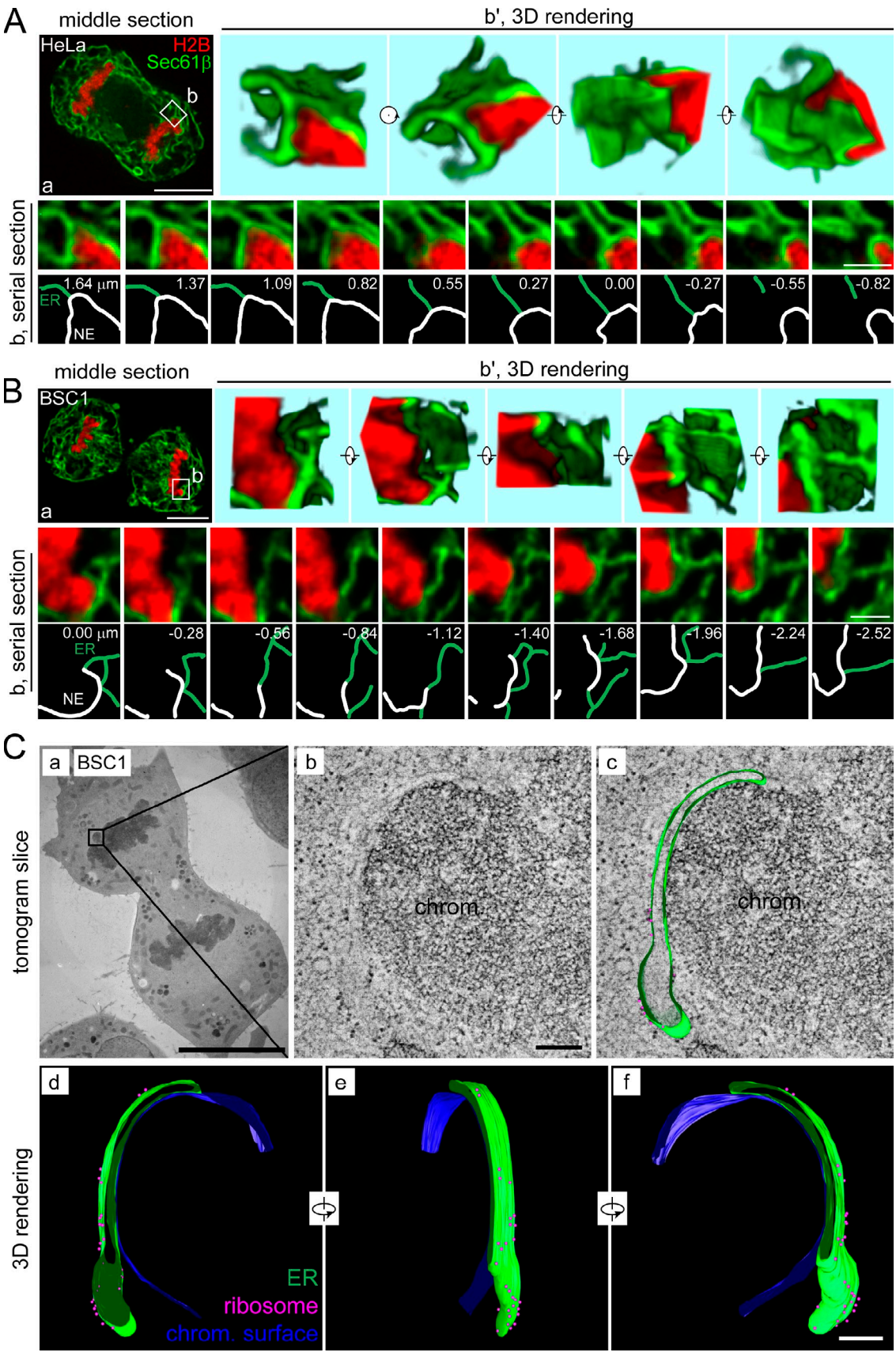

Figure 4. **Direct contribution of ER cisternae to assembly of the nuclear envelope.** (A and B) 3D renderings and serial optical sections show the relationship between the ER cisternae and nascent nuclear envelope in HeLa (A) and BSC1 (B) cells. 3D image stacks were acquired from mitotic cells expressing GFP-Sec61β and H2B-RFP. (a) Fluorescent image from the middle section. The boxed region contains an example of ER cisternae in continuity with the nascent

already attached to the chromosome mass, with the two membrane layers uniformly separated by the ∼50-nm spacing characteristic of the interphase nuclear envelope (Crisp and Burke, 2008) and with ribosomes only on the cytosolic side. Additional examples of EM tomograms of the nascent nuclear envelope with similar characteristics from BSC1 and IEC6 cells are shown in Fig. S3 (B and C). The resolution of the EM tomograms rules out the possibility that the nascent nuclear envelope originates by fusion of closely packed ER tubules.

Kinetics of the ER to nuclear envelope transformation

We took advantage of the known steady-state distribution of several ER and nuclear envelope membrane proteins during interphase and mitosis to assess the kinetics of their reassortment in the nascent nuclear envelope. Reticulons are membrane proteins excluded from the nuclear envelope and preferentially targeted to highly curved regions of the ER during interphase, including tubules and the edges of the cisternae (Voeltz et al., 2006). Nuclear envelope resident membrane proteins, such as LBR, emerin, and sun2, concentrate on the inner nuclear membrane. During mitosis, these proteins distribute evenly and colocalize with each other and with the ER membrane protein Sec61β (Ellenberg et al., 1997; Haraguchi et al., 2001; Anderson and Hetzer, 2007; Lu et al., 2009). By 2D live-cell imaging in mitotic HeLa cells, we followed the distribution of GFP-reticulon4a (Rtn4HD), GFP-emerin, GFP-LBR, or GFP-sun2 expressed along with mCherry-Sec61β. As expected, during anaphase, all of these proteins colocalized with ER cisternae (Fig. 2 and Fig. S2). The initial association of the ER with the rim of the chromosome mass began with the same protein content as in the mitotic ER followed by enrichment with resident nuclear envelope proteins and concomitant exclusion of reticulon4a, consistent with a previous study (Anderson and Hetzer, 2008). The relative content of Sec61β remained constant in both the ER and nuclear envelope (Fig. 2 and Fig. S2). After completion of nuclear envelope assembly, emerin (but not LBR or sun2) displayed a second phase of redistribution, switching from an even distribution to a polarized localization at the proximal and distal sides of the chromosome mass, ending again with a uniform distribution all around the chromosome mass (Fig. S2). The polarized location of emerin, followed by uniform redistribution, corresponds to an earlier observation by Haraguchi et al. (2000). Our substantially higher temporal resolution indicates that emerin, like the other nuclear membrane proteins, is first recruited to the rim and then accumulates on the proximal and distal sides of the chromosome mass. These observations suggest a dynamic sorting of the ER and nuclear envelope resident proteins during the postmitotic transformation from the ER into nuclear envelope.

Nuclear envelope formation always precedes assembly of nuclear pore complexes

The Nup107–160 complex is the first element of the nuclear pore complex known to associate with the chromosome mass during mitotic reassembly of nuclear pores (Belgareh et al., 2001; Harel et al., 2003; Walther et al., 2003; Antonin et al., 2005; Dultz et al., 2008). From ensemble data obtained by quantitative live-cell imaging, it has been proposed that, during early anaphase, the Nup107–160 complex assembles onto chromatin, forming the so-called prepore, followed by recruitment of POM121, a nuclear envelope membrane component of the nuclear pore complex (Dultz et al., 2008). From these observations, it was assumed that assembly of the prepore complex precedes formation of the nuclear envelope (Dultz et al., 2008). To aid the detection of nuclear pore complexes tracked as single objects, we increased the fluorescence signal to noise ratio by using triple GFP-tagged Nup133 (GFP×3-Nup133; Belgareh et al., 2001; Rabut et al., 2004). We found, by including Sec61β as a fluorescent marker for the nascent nuclear envelope, that formation of the nuclear envelope always preceded recruitment of the Nup107–160 complex (Fig. 5; Fig. S4, A and B; and Video 6). Our marker for the Nup107–160 complex, GFP×3-Nup133, was distributed with an even signal throughout the cytosol of mitotic cells that lacked a newly formed nuclear envelope and with a slight, diffuse accumulation within the chromosome mass relative to the cytosol (fluorescence intensity ratio of 1.20 ± 0.15, $n = 5$; Fig. 5, A and B) and as spots on kinetochores as reported previously (Fig. 5, D and E, open arrowheads; Belgareh et al., 2001; Zuccolo et al., 2007; Dultz et al., 2008). In contrast, GFP-Nup62, a soluble component of the nuclear pore recruited after the Nup107–160 complex, is excluded from the chromosome mass (fluorescence intensity ratio of 0.67 ± 0.05, $n = 6$; $P = 0.0008$; Fig. 5, A and B). Our results are consistent with previous studies in both mammalian cells and *Xenopus* in vitro reconstitution systems (Belgareh et al., 2001; Franz et al., 2007; Gillespie et al., 2007; Dultz et al., 2008; Rasala et al., 2008).

After the onset of nuclear envelope assembly, we observed new fluorescent GFP×3-Nup133 spots starting 80 ± 50 s ($n = 6$) after nuclear envelope initiation or 470 ± 20 s ($n = 5$) after the onset of anaphase but only at the rim of the chromosome mass, which was already occupied by the newly formed envelope tagged with mCherry-Sec61β (Fig. 5, C–E; Fig. S1 C; and Video 6). Similarly, two other components of the Nup107–160 complex, GFP-tagged Seh1 and GFP-tagged Nup37, were also recruited to the nascent nuclear membrane (Fig. 6, A and B). We confirmed the temporal relationship between the early recruitment of Nup133 with the delayed recruitment of Nup62 in HeLa cells simultaneously expressing GFP-Nup62 and tomato-Nup133 (Fig. S4, C and D). The onset of GFP-Nup62 recruitment

nuclear envelope and is further shown in b together with evenly spaced serial images along the z axis. The section at 0.00 µm corresponds to the optical section in a. b′ displays rendered 3D views of region b. The example highlights a direct contact between ER cisternae (green lines) and the nascent nuclear envelope (NE; white lines). (C) EM tomograms of the nascent nuclear envelope from an anaphase BSC1 cell. (a) Low magnification image of the whole cell. (b and c) A representative EM tomographic slice from the boxed region is shown without (b) and with (c) superimposition of a model for ER cisterna (green) and ribosomes (magenta). Chrom., chromosome mass. (d–f) Three views of the rendered 3D model. ER membrane, ribosome, and the surface of the chromosome mass are colored in green, magenta, and blue, respectively. Bars: (A–C, a) 10 µm; (A and B, b) 2 µm; (C, b and f) 200 nm.

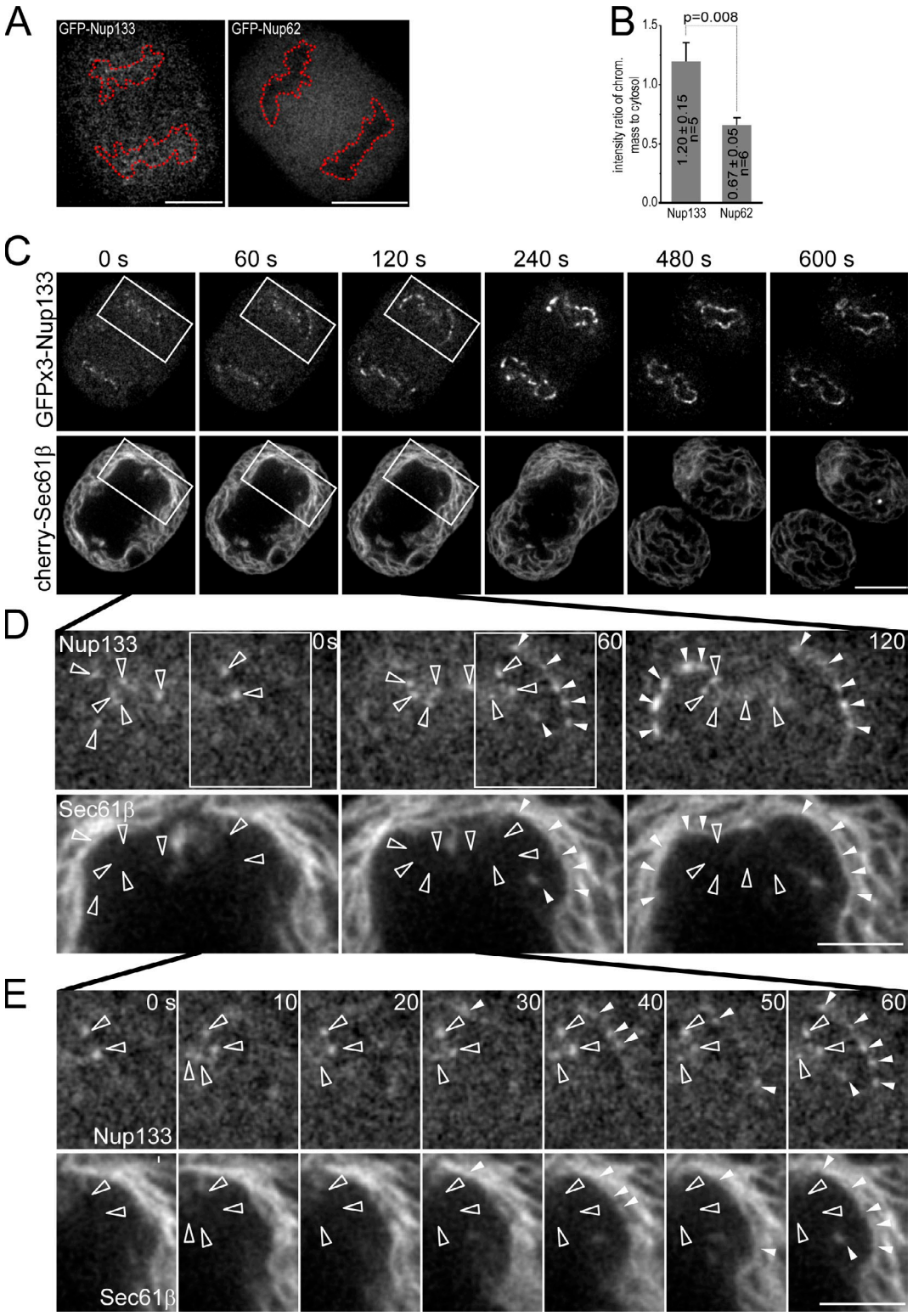

Figure 5. **Assembly of higher order Nup133 structures is restricted to the nascent nuclear envelope membrane.** (A) Association of Nup133, a component of the Nup107–160 complex, and Nup62 with the chromosome mass during early anaphase. The image is the middle section of a HeLa cell coexpressing GFP×3-Nup133 and H2B-mCherry (left) or GFP-Nup62 and H2B-mCherry (right) 30 s before its recruitment onto the nuclear envelope. The signal of H2B-mCherry (not depicted) was used to delineate the outer contours of the chromosome masses (dotted red lines). (B) Mean fluorescence intensity ratios ± SD of chromosome mass to cytosol for Nup133 and Nup62. The difference in ratios is statistically significant (P = 0.008). Chrom., chromosome. (C) A 2D time lapse from a mitotic HeLa cell expressing GFP×3-Nup133 and mCherry-Sec61β showing the recruitment of Nup133 onto the nuclear envelope (also see Video 6). The boxed regions are enlarged in D, and further enlarged boxed regions from D are shown in E. The onset of nuclear envelope formation is at 0 s. Open arrowheads show Nup133 associated with kinetochores. Closed arrowheads show Nup133 recruited to the nascent nuclear envelope. Note that Nup133 is absent on the surface of the chromosome mass at sites devoid of the nuclear envelope. Bars: (A and C) 10 µm; (D and E) 5 µm.

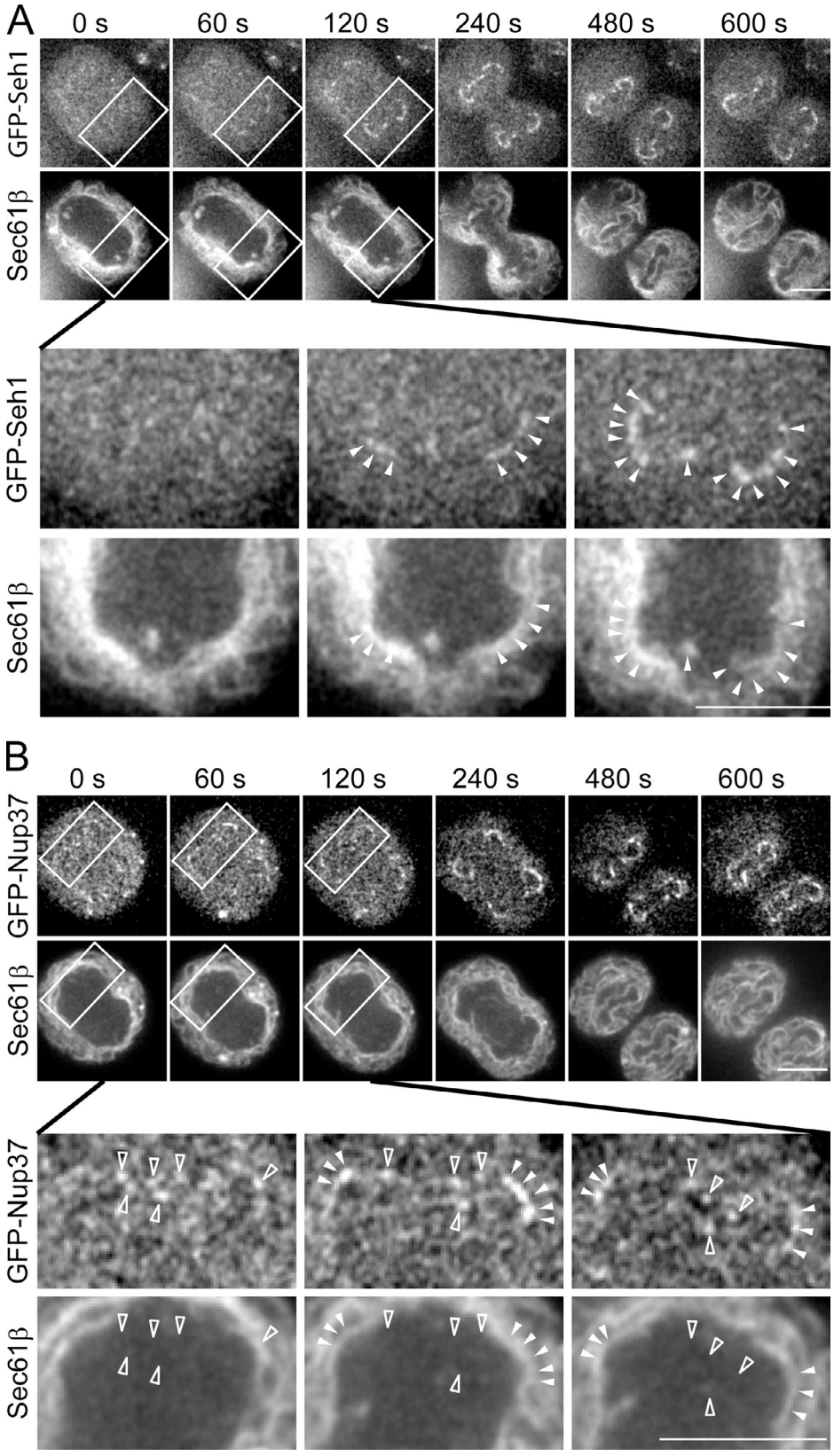

Figure 6. **Assembly of higher order Nup107–160 structures, visualized by imaging Seh1 or Nup37, is restricted to the nascent nuclear envelope membrane.** (A) 2D time lapse from a mitotic HeLa cell coexpressing GFP-Seh1 and mCherry-Sec61β showing the recruitment of Seh1 (closed arrowheads) onto the nuclear envelope. (B) 2D time lapse from a mitotic HeLa cell coexpressing GFP-Nup37 and mCherry-Sec61β showing the recruitment of Nup37 (closed arrowheads) onto the nuclear envelope. Open arrowheads indicate kinetochores. See legend of Fig 5 (C and D) for a detailed description. Boxes in A and B are enlarged at the bottom. Bars, 10 μm.

occurred ~3 min after nuclear envelope initiation, delayed by 110 ± 30 s (n = 4) with respect to Nup133 recruitment (Fig. S4, C and D). All the spots containing Nup62 colocalized with Nup133, in agreement with the sequential assembly of nuclear pore complexes as previously suggested (Dultz et al., 2008). These results strongly suggest that the assembly of nuclear pores occurs on the preformed nuclear envelope.

To test directly whether the fluorescent spots of GFP×3-Nup133 associated with the nascent nuclear envelope corresponded to nuclear pores, we first calibrated the fluorescence intensity of a triple GFP molecule by determining the mean fluorescence of single spots visualized on a glass coverslip containing a dilute solution of cytosol from cells expressing σ2-GFP (a monomeric subunit of the clathrin adaptor AP-2 complex) or GFP×3 (Fig. S5). Single spots of σ2-GFP (Fig. S5 A) displayed ~1/3 of the fluorescence signal generated by GFP×3 (Fig. S5 B), thus providing the required single-molecule intensity calibration. We then imaged fixed cells expressing low levels of GFP×3, H2B-mCherry, and mCherry-CAAX at interphase and quantitatively determined the amount of GFP×3 associated with a given fluorescent spot (Fig. S5 C). The mean fluorescence intensity of the spots imaged throughout the cytosol was equivalent to the fluorescence intensity measured for the single GFP×3 molecules, therefore providing additional quantitative validation of the intensity measurements. As a further control, we imaged interphase nuclear pores (Fig. 7 A), which are known to contain 16 copies of Nup107–160 complexes (Cronshaw et al., 2002; Rabut et al., 2004). The histogram in Fig. 7 A corresponds to the GFP×3-Nup133 content in nuclear pores on the bottom of the nuclear envelope and is obtained after normalization by the fluorescence intensity expected for a triple GFP molecule. We found that the mean GFP×3-Nup133 content per nuclear pore complex was 7.6 ± 3.4 (n = 1,690 from 16 cells), suggesting that in the interphase pores, ~50% of the newly assembled Nup133 had been replaced by GFP×3-Nup133. We then analyzed GFP×3-Nup133 in fixed anaphase and telophase cells (Fig. 7, B–F), focusing on the following locations (Fig. 7 C): the cytosol (Fig. 7 C, cytosol), the region of chromosome mass lacking the nuclear envelope, including the spindle pole distal side and the interior of the chromosome mass (Fig. 7 C, chrom.), the region of chromosome mass where the nascent nuclear envelope forms (Fig. 7 C, rim), and the region occupied by kinetochores, including the spindle pole proximal side (Fig. 7 C, kinetochore). For the cell in Fig. 7 B, the recruitment of Nup133 at the rim had just occurred at the time the cells were fixed (Fig. 7 B, arrowheads). Relatively weak single spots in the cytosol and on the chromosome masses contained 0.84 ± 0.64 (n = 70) and 0.93 ± 0.67 (n = 92) copies of GFP×3-Nup133, respectively (Fig. 7 D, cytosol and chrom.), consistent with the view that at this stage, Nup107–160 complexes are in single units rather than higher order prepore structures. The spots at the rim of the chromosome mass in early anaphase, before significant recruitment of Nup133, contained 1.1 ± 0.6 (n = 93) GFP×3-Nup133 (Fig. 7 E), skewing at later times toward a distribution with a subset peaking at a higher GFP×3-Nup133 content (Fig. 7 D, rim). In contrast, during telophase, the spots at the rim had on average 2.7 ± 1.2 GFP×3-Nup133 molecules, with a subset showing a distribution peaking at approximately four GFP×3-Nup133 molecules (Fig. 7 F). This distribution is consistent with the expected combined content of GFP×3-tagged Nup133 and endogenous Nup133 in newly assembled postmitotic nuclear pores, as they should contain on average ~50% of the GFP×3-Nup133 content of premitotic nuclear pores. This dilution is the result expected if all Nup107–160 complexes contained in the fluorescent and nonfluorescent old pores contribute to the formation of all postmitotic nuclear pores. Finally, the fluorescent spots identified in the kinetochore region contain on average 6.1 ± 1.7 (n = 76; Fig. 7 D, kinetochore) or 5.7 ± 2.1 (n = 410 from nine cells; Fig. S5 D) GFP×3-Nup133 molecules. The relative intensity of these signals was also used as an internal calibration to show the restricted appearance of bright Nup133 spots on the nascent nuclear envelope during live-cell imaging (Fig. 5, C–E). Together, these observations indicate that Nup107–160 complexes associate with the chromosome mass as single units rather than the formation of prepores before the assembly of the nuclear envelope. They also show that assembly of the nuclear pore is restricted to regions of the chromosome mass associated with the nascent nuclear envelope.

Spatial and temporal relation of postmitotic nuclear import and nuclear envelope formation

The import of nuclear cargo was followed by live-cell imaging of a chimeric protein made of importin-β binding domain (IBB) fused to tomato (IBB-tomato) in cells coexpressing GFP-Sec61β (Fig. 8 A). During interphase, IBB undergoes efficient nuclear import through nuclear pore complexes. Upon mitotic nuclear envelope breakdown, it is released into the cytosol (Dultz et al., 2008). The times for recruitment of Nup133, Nup62, and Sec61β and for IBB import are shown as plots in Fig. 8 B (also see Fig. S1). Nuclear accumulation of IBB occurred 620 ± 50 s (n = 5) after the onset of anaphase, at a time when ~3/4 of the nuclear envelope had already assembled (Fig. 8 A). IBB accumulation always began at the rim of the chromosome mass close to the region where the nuclear envelope and pore assembly initiated (Fig. 8 A, IBB onset). The results were unexpected because there are clear gaps in the nuclear envelope between the cytosol and the chromosome mass (Fig. 8 A, arrowheads). These observations highlight the need to use the nuclear envelope rather than IBB import as a temporal reference for the nuclear envelope assembly because onset of IBB import cannot be equated with completion of the postmitotic nuclear envelope as it was assumed in previous studies (Anderson and Hetzer, 2008; Dultz et al., 2008).

Discussion

We have shown here, using 2D and 3D live-cell imaging with confirmation from high-resolution EM tomography, that ER cisternae are the main contributors to the postmitotic formation of the nuclear envelope. We have also demonstrated that the presence of the nuclear envelope is essential for the postmitotic assembly of nuclear pores. We have found no evidence for the formation of prepores in those regions of the mitotic chromosome mass devoid of the nuclear envelope.

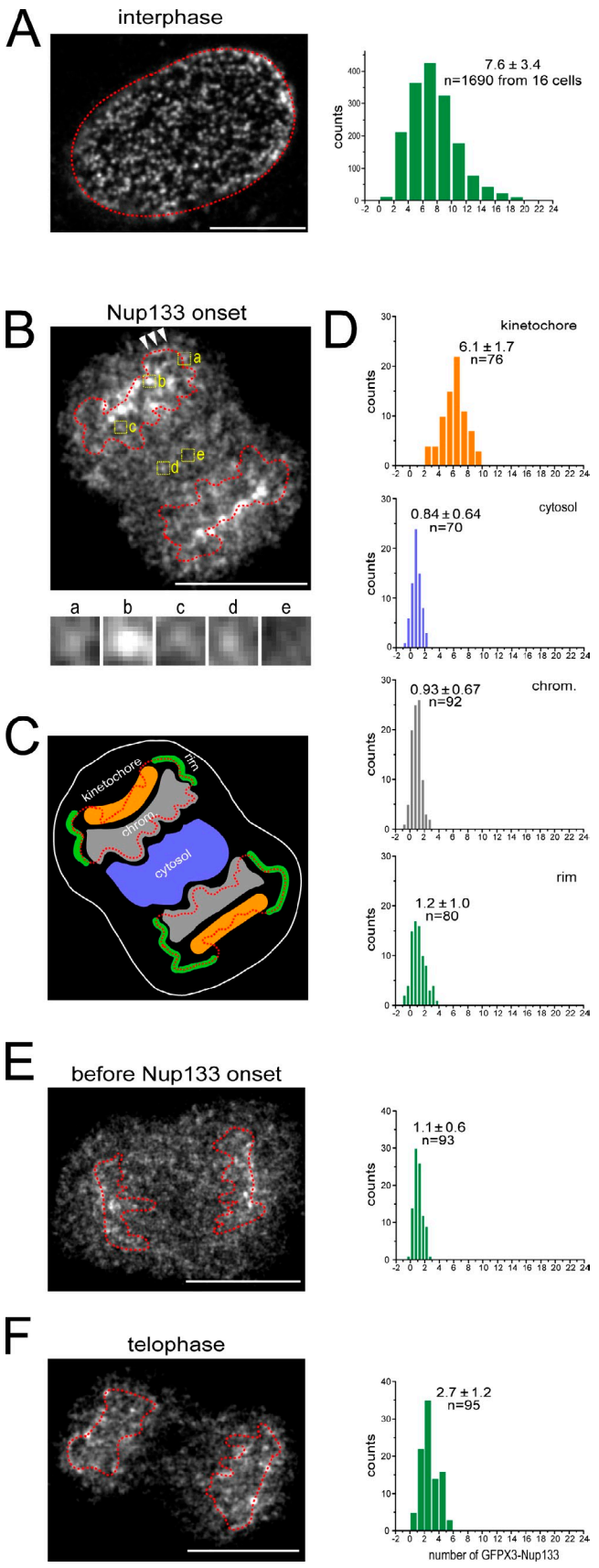

Figure 7. **Quantification of GFP×3-Nup133 during the postmitotic nuclear pore assembly.** HeLa cells coexpressing GFP×3-Nup133 and H2B-mCherry (not depicted) were chemically fixed and then imaged in 3D. Contours around the chromosome masses and nuclei were established by following the location of the H2B-mCherry fluorescence signal (dotted red lines). (A) Interphase nuclear pores. The image is from a nuclear envelope located at the bottom side of nucleus close to the glass coverslip. Fluorescence intensity distribution of 1,690 GFP×3-Nup133 spots imaged in 16 cells. The data represent the results from 16 cells. (B) Image from the middle section of a cell in anaphase acquired during the initial stages of Nup133 recruitment. The yellow boxes contain diffraction-limited fluorescent spots acquired from (a) rim region, (b) kinetochore region, (c) chromosome mass, (d) cytosol, and (e) control region without objects (background). Nondiffraction-limited objects (arrowheads) were excluded from the analysis. (C) Schematic representation of the regions used for analysis. (D) Fluorescence intensity distribution of diffraction-limited spots from each of the four regions color coded as indicated in C. (E) Image from the middle section of a cell in anaphase before the onset of Nup133 recruitment to the nuclear envelope and fluorescence intensity distribution of diffraction-limited Nup133 spots at the rim of the chromosome mass. (F) Image from the middle section of a cell in telophase and fluorescence intensity distribution of diffraction-limited Nup133 spots at the rim of the chromosome mass. Note the appearance of a population of spots peaking at approximately four GFP×3-Nup133. In B–D, the data represent the results from three cells. Chrom., chromosome. Bars, 10 µm.

In our previous work, we followed the distribution of ER and nuclear envelope markers during mitosis using live-cell imaging (Lu et al., 2009). We concluded that during mitosis, most of the ER is organized as extended cisternae or sheets present throughout the cytosol but are excluded from the spindle region, with a very small fraction of the ER remaining as tubules along the spindle microtubules. The prevalence of extended ER cisternae during mitosis led us to investigate whether these ER cisternae, rather than tubules, are the source of membrane for the formation of the postmitotic nuclear envelope. The Sec61β pattern within a single optical section always appears as a smooth curvilinear tracing connecting the ER within the cytosol to a membrane immediately adjacent to the chromosome mass. The membrane associated with the chromosome mass is enriched in the nuclear resident proteins LBR, sun2, and emerin and depleted of the ER protein reticulon4a, consistent with its transformation from the ER to the nuclear envelope. Earlier, we demonstrated that the curvilinear tracings correspond to optical sections of extended cisternae (Lu et al., 2009). These observations indicate that the nuclear envelope arises directly from cisternal rather than tubular ER. This interpretation is in full agreement with our high-resolution EM tomographic observations from mitotic cells showing profiles corresponding to the nascent nuclear envelope contiguous with ER cisternae but not tubules. An important prediction from these observations is that the absence of ER tubules should not affect postmitotic nuclear envelope formation. To test this idea, we took advantage of the observation that during interphase, acute microtubule depolymerization leads to the rapid and complete conversion of ER tubules into cisternae (Lu et al., 2009). Likewise, treatment with nocodazole at anaphase leads to the rapid loss of the spindle microtubules, whereas formation of the postmitotic nuclear envelope still proceeds, consistent with the notion that ER tubules do not represent an important source of ER membrane for nascent nuclear envelopes.

Hetzer's group has proposed an alternative model, suggesting that ER tubules first attach to the chromosome mass followed by a lateral expansion on the surface of the chromosome

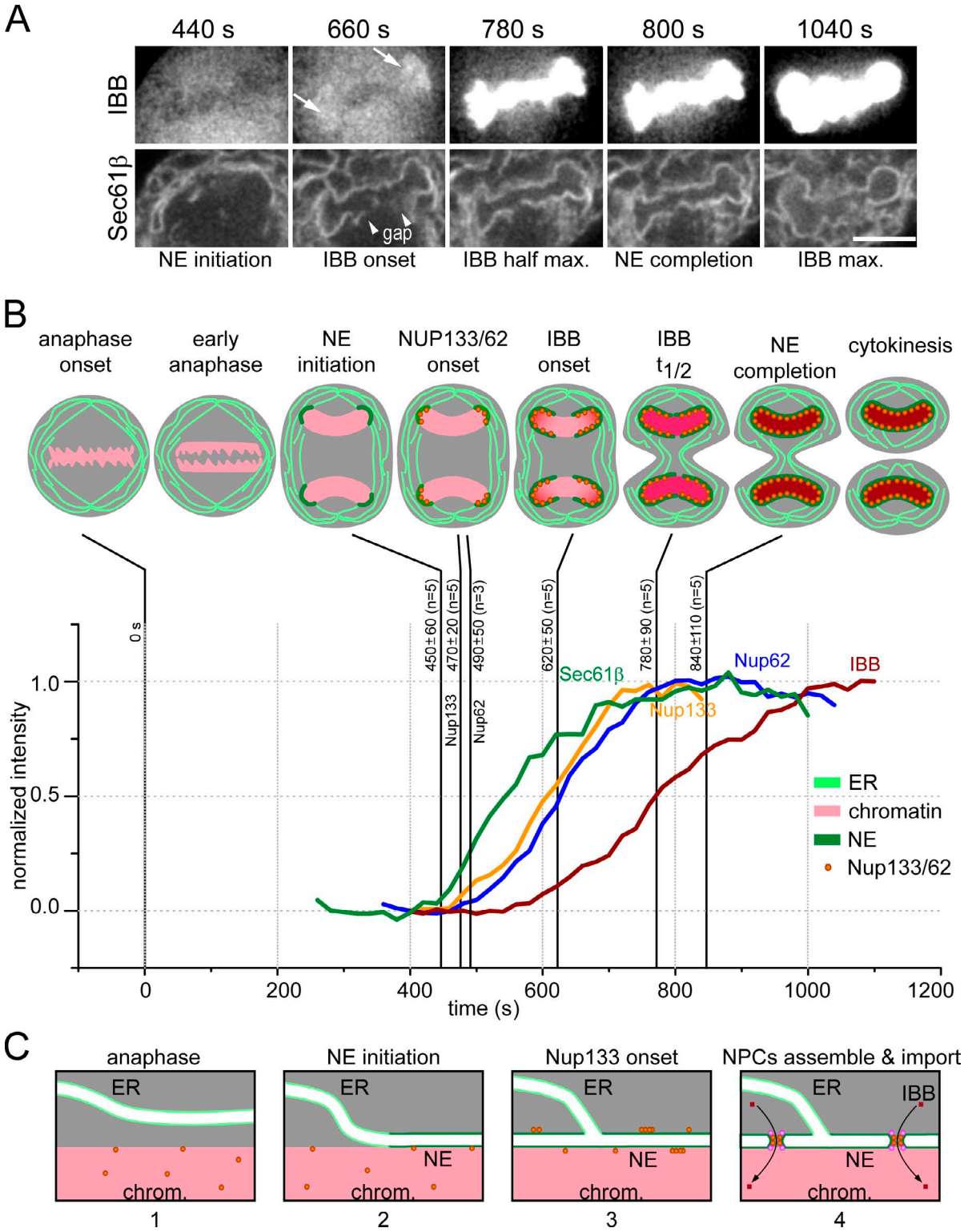

Figure 8. **Postmitotic import of IBB, summary of kinetic results obtained in this study, and working model for the postmitotic assembly of the nuclear envelope and nuclear pores.** (A) 2D time lapse of a mitotic HeLa cell expressing GFP-Sec61β and IBB-tomato acquired during nuclear envelope assembly (also see Video 7). Anaphase onset is at 0 s. At 660 s, imported IBB was clearly visualized next to the rim of the chromosome mass (arrows), at a time when assembly of the nuclear envelope is still incomplete as highlighted by the gap between the arrowheads. Key events were obtained by quantification of the Sec61β and IBB fluorescence signals. Bar, 10 µm. (B) Schematic summary of the relative kinetics of nuclear envelope formation and nucleoporin recruitment. The plots represent the fluorescence intensity associated with formation of the nuclear envelope (Sec61β, green; Fig. S1 B), recruitment of Nup133 (yellow; Fig. S1 C), recruitment of Nup62 (blue; Fig. S1 D), and import of IBB (red; Fig. S1 E). (C) Working model for the postmitotic assembly of the nuclear envelope and nuclear pores. ER is shown in light green; nuclear envelope (NE) is shown in dark green; yellow dot shows Nup107–160 complex; magenta dot shows remaining component of the nuclear pore; red square shows IBB; Chrom., chromosome mass.

mass to generate the nuclear envelope (Anderson and Hetzer, 2007, 2008; Anderson et al., 2009). Such a direct role for ER tubules is unlikely, considering their relative scarcity with respect to the cisternal ER and in view of the observations described in this paper. In an in vitro nuclear envelope membrane reconstitution assay, they found that a network of preformed ER tubules is the source for newly assembled nuclear envelope membrane (Anderson and Hetzer, 2007). It remains to be established, however, whether such an in vitro preparation can represent the in vivo mechanism with fidelity. We propose that extended ER cisternae are the main membrane source for the mitotic biogenesis of the nuclear envelope membrane. Reticulons are proteins that partition preferentially to highly curved ER membranes and are depleted from the low curvature nuclear envelope membrane. Overexpression of reticulons has been reported to deplete ER cisternae and stabilize ER tubules (Voeltz et al., 2006). Indeed, our model is consistent with a previous finding showing delayed nuclear envelope formation in cells overexpressing reticulons and an accelerated formation in cells depleted of reticulons (Anderson and Hetzer, 2008). It is also known that interaction of nuclear membrane proteins with the chromatin helps provide the driving force for membrane migration (Anderson et al., 2009); it is possible that presence of abnormally high amounts of reticulons on the growing nuclear envelope membrane slows this process. Finally, it has been argued that tubular ER is the source for the nuclear envelope membrane because of its observed abundance in thin-section EM of chemically fixed mitotic cells (Puhka et al., 2007). We have shown, however, that in cells undergoing mitosis, most of the ER becomes an interconnected network of cisternae conspicuously lacking tubules and that the chemical fixation normally used to visualize EM results in cisternal fenestration and apparent tubulation (Lu et al., 2009).

Evidence in favor of a prepore model comes indirectly from in vitro studies (Comings and Okada, 1970; Maul, 1977; Sheehan et al., 1988; Bodoor et al., 1999; Walther et al., 2003; Antonin et al., 2005) and from more recent evidence by live-cell imaging (Dultz et al., 2008). In their live-cell imaging study, Dultz et al. (2008) used ensemble measurements to follow the accumulation of the Nup107–160 complex tagged with GFP×3-Nup 133 and of the membrane-bound nucleoporin POM121 on the surface of the chromatin mass. They observed that the onset of Nup133 accumulation precedes, by a few minutes, the recruitment of POM121 by calibrating the recruitment kinetics of these nucleoporins with respect to the nuclear import of IBB (Dultz et al., 2008). Direct association of soluble nucleoporins with the nuclear membrane would be possible even if POM121, gp210, or NDC1 has not yet been recruited because mammalian Nup133 and yeast Nup53 and 59, components of the Nic96 scaffold complex, can associate with liposomes in vitro (Drin et al., 2007; Patel and Rexach, 2008). In agreement with this possibility, it has now been shown, using knockdown approaches, that embryonic large molecule derived from yolk sac (ELYS), but not POM121, plays a critical and essential role in the recruitment of the Nup107–160 complex to chromatin and in the assembly of postmitotic nuclear pores (Rasala et al., 2006, 2008; Franz et al., 2007; Gillespie et al., 2007; Doucet et al., 2010). These observations do not exclude the possibility that POM121 can be nucleated to regions already containing Nup107–160. Doucet et al. (2010) also showed that during interphase, POM121, but not ELYS, is essential for nuclear pore assembly. Indeed, the recent live-cell imaging by Dultz and Ellenberg (2010), performed with a time resolution of 5–15 min using interphase cells simultaneously expressing fluorescently tagged POM121 and Nup133, showed that recruitment of POM121 to a forming nuclear pore precedes the arrival of Nup133. The kinetics of postmitotic pore formation was ∼10 times faster when compared with the formation of nuclear pores during interphase.

Our data, based on single-particle tracking calibrated for fluorescence intensity, do not support the prepore model. We find that the nuclear envelope membrane, labeled by Sec61β, is always present at sites of Nup133 assembly. The fluorescence signal of GFP×3-Nup133 associated with chromatin devoid of nuclear membrane always corresponded to nonassembled single units, in agreement with recent electron microscopy observations showing association of single Nup107–160 complexes with chromosome masses in vitro (Rotem et al., 2009). In contrast, postmitotic Nup107–160 assemblies associated with the nascent nuclear membrane contained approximately four GFP×3-Nup133, which we interpret as single nuclear pores. This assignment is consistent with the replacement of endogenous Nup133 with GFP×3-Nup133, the value expected after reassortment of Nup133 after mitotic dissolution and reassembly from fluorescently tagged and nontagged interphase nuclear pores.

An insertion model for the postmitotic assembly of nuclear pores has the conceptual advantage of unifying the mechanisms of postmitotic and interphase pore formation. We can combine the results reported here with published observations to propose a more specific picture (Fig. 8 C). In particular, we suggest that insertion is a symmetrical process, involving apposition of Nup107–160 complexes on both inner and outer nuclear membranes, corresponding to the symmetrical arrangement of the two eightfold rings of these complexes in the mature structure. During early anaphase, individual Nup107–160 complexes associate with the chromosome mass through an interaction mediated by ELYS. In midanaphase, a double membrane derived from ER cisternae adheres to the chromosome mass and begins to spread over its surface. Prerecruitment of Nup107–160 ensures that a set of these complexes will be present on the nuclear side of the nascent nuclear envelope and indicates that at least part of the insertion process comes from within. The presence of POM121 (or another nuclear membrane–bound protein that remains to be determined) on the inner nuclear membrane can help cluster Nup107–160 complexes into higher order ring structures, corresponding to early stages of pore formation. A similar process, nucleated by POM121 on the outer membrane, can recruit Nup107–160 from the cytosol into rings on the outer membrane. Pore formation then requires apposition of inner and outer membrane rings and localized luminal membrane fusion. The spacing between inner and outer nuclear membranes is 30–50 nm, and the luminal tail of POM121 is too short (∼30 aa) to be the driving force for fusion. Transient interaction of the POM121 tails with an intraluminal protein yet

to be determined might bring together the two membranes at the position of an inner Nup107–160 ring, help nucleate a corresponding POM121/Nup107–160 ring on the outer membrane, and potentially "snap" together the two rings, driving membrane fusion within them. During interphase, a comparable process probably would require the import of the Nup107–160 complex through existing nuclear pores.

Materials and methods

Plasmids

The expression vectors encoding Sec61β in pAcGFP1-C1, Sec61β in pmCherry-C1, tubulin in pmCherry-C1, LBR in pAcGFP1-N1, reticulon4a (Rtn4HD) in pAcGFP1-C1, emerin in pEGFP-N1, and pBABE X-H2B-mRFP1 have been used as previously described (Lu et al., 2009). Sun2-GFP was a gift from B. Burke (Institute of Medical Biology, Singapore). GFP-Nup37 and GFP-Seh1 were gifts from I.M. Cheeseman (Whitehead Institute, Massachusetts Institute of Technology, Boston, MA).

To clone H2B into pmCherry-N1, pBOS-H2B-GFP (BD) was digested with SalI–BamHI and then ligated into pmCherry-N1 (Takara Bio Inc.). To construct GFP-Nup133, the pEGFP-C1 vector (Takara Bio Inc.) was first modified to introduce a NotI site between the SacII and BamHI sites. The coding sequence of human Nup133 was obtained from the IMAGE (Integrated Molecular Analysis of Genomes) clone (available from GenBank/EMBL/DDBJ under accession no. BC020107) using SacII–NotI and ligated into the modified pEGFP-C1 vector using the same restriction sites. To construct Nup133 in ptdTomato-C1, the plasmid Nup133 in the modified pEGFP-C1 was released with EcoRI–BamHI and then ligated into the ptdTomato-C1 vector. To construct a triple GFP vector (pEGFPx3-C1), two copies of the coding sequence of EGFP were sequentially amplified by PCR and then inserted into the pEGFP-C1 vector using BglII–HindIII and HindIII–EcoRI sites. To construct GFPx3-Nup133, the Nup133 fragment was released from GFP-Nup133 by EcoRI–BamHI digestion and subsequently ligated into pEGFPx3-C1 vector. To construct GFP-Nup62, the coding sequence of human Nup62 was released from the IMAGE clone (GenBank accession no. BC050717) using SalI–NotI and ligated into the modified pEGFP-C1 vector. Because the 5′ end sequence of the Nup62 fragment is not compatible with the reading frame of the vector, the 5′ fragment was removed by XhoI–EcoRI digestion and replaced by an XhoI–EcoRI-digested PCR product, which was generated by using primers 5′-GACTCACTCGAGACAGCGGGTTTAATTTTGGAGG-3′ and 5′-CTGGGCTGAATTCCCTGCTGAG-3′ and the Nup62 IMAGE clone as the template. To make the plasmid expressing IBB-tomato, the IBB of human importin-α was PCR amplified from the IMAGE clone (GenBank accession no. BC035090), and the PCR product was ligated into ptdTomato-N1 vector (Takara Bio Inc.) at EcoRI–BamHI sites. To make the plasmid expressing mCherry with the C-terminal CAAX motif for plasma membrane localization, primers 5′-AATTCAGGCTGCATGAGCTGCAAGTGTGTGCTCTCCTGAG-3′ and 5′-GATCCTCAGGAGAGCACACACTTGCAGCTCATGCAGCCTG-3′ were annealed and ligated into pmCherry-C1 at EcoRI and BamHI sites. All constructs were verified by DNA sequencing.

Reagents and cell culture procedures

Nocodazole and taxol were purchased from Sigma-Aldrich. Cell culture and transfection procedures were conducted as previously described (Lu et al., 2009). In brief, HeLa, BSC1, 293, and IEC6 cells were grown in DME supplemented in 10% fetal bovine serum at 37°C and in the presence of 5% CO_2. Transient expression in HeLa, BSC1, or 293 cells of the chimera proteins was performed using Lipofectamine 2000 (Invitrogen). 3 h after transfection, the cells were replated in small Petri dishes containing a glass bottom (no. 1.5; MatTek Corporation) and allowed to grow for ∼20 h in fresh medium before imaging.

Fluorescence imaging

Live-cell spinning-disk confocal microscopy in 2D and 3D was performed as previously described (Lu et al., 2009). Cells grown on the glass-bottom Petri dish were imaged using CO_2-independent medium (Invitrogen) supplemented with 10% fetal bovine serum and 2.5 mM L-glutamine. The Petri dish was placed in an enclosed environment chamber surrounding the microscope stage set to 37°C. The fluorescent images were acquired using a Marianas system under control of SlideBook (version 4.0; Intelligent Imaging Innovations). The system was based on an inverted motorized microscope (Axiovert 200M; Carl Zeiss) equipped with a 63×, NA 1.4 Plan Apochromatic objective (Carl Zeiss), a piezo-driven stage (Applied Scientific Instrumentation), a spinning-disk confocal head (CSU22; Yokogawa), a computer-controlled spherical aberration correction device (Infinity Photo-Optical), and an electron-multiplying charge-coupled camera (Cascade 512B; Photometrics) set to speed = 1, gain = 3, and amplification = 4,095. Each pixel on the final imaged mapped to 0.093 × 0.093 µm. The samples were illuminated with 50-mW solid-state lasers whose emission wavelengths were centered at 472 and 561 nm; each frame corresponding to dual-wavelength acquisitions was acquired sequentially at 472 and 561 nm using an acousto-optic tunable filter for wavelength selection. Unless indicated otherwise, the exposure time was ∼100 ms per wavelength. 2D time series were acquired every 5–30 s. 3D z stacks were acquired every 500 –700 ms using steps of 0.09–0.28 µm. The refractive index mismatch between the sample (water) and the immersion oil generates an apparent elongation of the image along the z axis, which was corrected using a factor of 0.7 calculated by imaging fluorescent spherical beads of 15 µm in diameter (Invitrogen; Ferko et al., 2006). All z distances have been corrected accordingly.

Image analysis

Image filtering, segmentation, morphometry, and determination of fluorescence intensity were performed using SlideBook version 4.0. Image restoration by 3D deconvolution was performed using Huygens Essential software (version 3.3; Scientific Volume Imaging). 3D rendering of nuclear envelopes was performed on deconvolved 3D image stacks of cells expressing Sec61β and H2B on a 3D mask defined by the segmented signal of H2B (see Fig. S1 A for an example). The mask was dilated by 4 pixels, converted to a binary 3D image, and then multiplied logically to the Sec61β signal. 3D rendering was performed using Volocity software (version 2.6.3; PerkinElmer). 2D time lapses of live cells and 3D image stacks of fixed cells were Gaussian filtered (σ = 1 pixel). For quantitative analysis, 2D time lapses were background subtracted and corrected for photobleaching.

The data from each time point was normalized and plotted against time. In Fig. 2, the mask of the nuclear envelope was manually traced along a rim region where the enrichment of LBR-GFP or the depletion of GFP-Rtn4HD occurred. The mask of the ER was similarly generated on a segment of GFP-Sec61β–labeled ER membrane profile outside the central cavity. In Fig. 5 (A and B), masks were segmented using H2B-mCherry intensity or manually drawn over cytosol region, and mean intensities of Nup133 and Nup62 at both masks were obtained subsequently. For Nup133, kinetochores were manually removed from the chromosome mass mask. In Fig. S1, various dynamic processes were analyzed using 2D time lapses. To analyze the nuclear envelope recruitment in Fig. S1 B, a binary mask of the chromosome mass is first generated by segmenting H2B-mCherry intensity and subsequently dilated by 5 pixels as illustrated in Fig. S1 A. The nuclear envelope mask is selected by logically multiplying the GFP-Sec61β image with the binary mask. The GFP-Sec61β fluorescent intensity within the nuclear envelope mask was summed at each time point and used as the relative amount of recruited nuclear envelope membrane. To analyze the recruitment of Nup133 or Nup62 in Fig. S1 (C or D), respectively, a mask was generated by segmenting GFP-Nup133 or Nup62 signal during nuclear envelope assembly, and the summed intensity was used as the relative amount of recruited nucleoporin. To analyze the import of IBB in Fig. S1 E, masks of chromosome masses were manually traced at each time point using the IBB-tomato image by taking advantage of the contrast between the chromosome mass and cytosol. In contrast to the cytosol, the chromosome mass appeared dark before IBB import and bright after the import. The relative amount of imported IBB was obtained by summing IBB intensity within the chromosome mass mask. Each printed image is a representative example of the experiment obtained from a single cell. Confirmatory data (unpublished data) was obtained by imaging at least two additional cells. Statistical analysis was performed using OriginPro8 software (OriginLab).

Calibration of single GFP and GFP×3 fluorescence intensities

BSC1 cells stably expressing σ2-GFP (cloned in pEGFP-N1), a component of the endocytic clathrin adaptor complex AP-2 (Ehrlich et al., 2004), or HeLa cells transiently expressing GFP×3 (pEGFPx3-C1) were broken by repeated extrusion through a 27-gauge needle. The lysate was centrifuged at 100,000 rpm at 4°C in a rotor (TLA-100; Beckman Coulter) using an ultracentrifuge (Optima TLX; Beckman Coulter). Diluted supernatant was applied to the top of a glass coverslip (no. 1.5), air dried, and mounted on a glass slide using Mowiol 488 (EMD) with 0.3% 1,4-diazabicyclo [2.2.2] octane (DABCO; Sigma-Aldrich), which was used as an antiphotobleaching

agent. Photobleaching tracings of diffraction-limited fluorescent spots corresponding to single GFP or GFP×3 molecules were acquired from 2D time-lapse imaging series (700-ms exposure; camera setting: speed = 1, gain = 3, and amplification = 3,800). The background-corrected tracings show summed intensities within a 7 × 7–pixel (0.61 × 0.61 µm) mask centered on the diffraction-limited fluorescent spot. The fluorescence intensity of GFP or GFP×3 was calculated as the difference of intensities before and after photobleaching using ImageJ (National Institutes of Health).

Measurement of GFP×3-Nup133 intensity in fixed cells

HeLa cells transiently expressing GFP×3-Nup133 together with H2B-mCherry were fixed with 4% paraformaldehyde and mounted in Mowiol 488 with 0.3% DABCO. Cells were imaged as 3D stacks (z spacing of 0.14 µm) using the same camera settings as for the calibration of single molecules and an exposure of 350 ms. The optical section containing the strongest fluorescent signal for any given spot was selected, and the fluorescence intensity of the spot was determined by first summing the intensity within a 7 × 7–pixel mask and then subtracting the background outside the mask. The number of GFP×3-Nup133 contained within a given diffraction-limited spot was calculated as (700 ms/350 ms) × (intensity of a diffraction limited spot)/(mean intensity of a single GFP×3).

EM sample preparation and electron tomography

For electron tomographic experiments, samples were prepared and imaged as previously described (Lu et al., 2009). Cells were grown on carbon-coated synthetic sapphire disks (3.0-mm diameter and 0.07-mm thickness; Rudolf Brügger SA). The disks were made hydrophilic by glow discharging and UV sterilized just before use. Disks with confluent cell monolayers were placed in aluminum planchettes that had been prefilled with hexadecene (an external cryoprotectant) and rapidly frozen in a high-pressure freezer (Bal-Tec HPM 010; Leica). The vitreous samples were then freeze substituted into 2.5% OsO_4 in acetone at −90°C for 5 d, warmed to −20°C over 48 h, and then warmed to 4°C over 1 h. Samples were rinsed 3× with cold acetone, infiltrated with Epon-Araldite resin (Electron Microscopy Sciences), and flat embedded between a glass slide and a plastic coverslip. Resin was polymerized at 60°C for 48 h. The embedded samples were observed with a phase-contrast light microscope (Diaphot 200; Nikon) equipped with 10×, 20×, and 40× objective lenses to select appropriate regions of cells for analysis. These areas were excised from the resin block and remounted onto plastic sectioning stubs with a two-part epoxy adhesive (Epoxy 907; Miller-Stephenson Chemical Company, Inc.). Semithick (200 nm) sections were cut with either an Ultracut UCT or EM UC6 ultramicrotome (Leica) using a diamond knife (Diatome). Serial sections were collected onto Formvar-coated copper-rhodium slot EM grids (Electron Microscopy Sciences) and stained with uranyl acetate and lead citrate. Colloidal gold particles (10 or 15 nm; British Biocell International or Sigma-Aldrich) were placed on both surfaces of the grid to serve as fiducial markers for subsequent image alignment. Sections were imaged with either a Tecnai TF20 (200 keV) or Tecnai T12 (120 keV) transmission electron microscope (FEI Company). Images were recorded digitally with a charge-coupled device (UltraScan; Gatan, Inc.). Dual-axis tilt series datasets were acquired as previously described (Mastronarde, 1997) using the SerialEM software package (Mastronarde, 2005). Tomographic reconstructions were calculated, analyzed, and modeled using the IMOD software package (Kremer et al., 1996) on a Macintosh G5 or MacPro computer (Apple, Inc.).

Online supplemental material

Fig. S1 shows the kinetics of assembly of the nuclear envelope, recruitment of Nup133 and Nup62, and import of IBB. Fig. S2 shows accumulation of emerin and sun2 on the nascent nuclear envelope. Fig. S3 shows direct contribution of ER cisternae to the assembly of the nuclear envelope. Fig. S4. shows that sequential assembly of Nup133 and Nup62 during mitosis occurs on the nascent nuclear envelope. Fig. S5 shows calibration of the fluorescence intensity of GFP and GFP×3. Video 1 shows the dynamics of mitotic nuclear envelope assembly from ER cisternae. Video 2 shows the dynamics of mitotic nuclear envelope assembly in a BSC1 cell. Video 3 shows the dynamics of spindle microtubules and nuclear envelope assembly. Video 4 shows the effect of nocodazole on the dynamics of spindle microtubules and nuclear envelope assembly. Video 5 shows the effect of taxol on the dynamics of spindle microtubules and nuclear envelope assembly. Video 6 shows the dynamics of mitotic assembly of Nup133 relative to the nascent nuclear envelope. Video 7 shows the dynamics of IBB import during nuclear envelope assembly. Online supplemental material is available at http://www.jcb.org/cgi/content/full/jcb.201012063/DC1.

We thank Eric Marino for maintaining the imaging resource used in this study, Brian Burke and Iain M. Cheeseman for generously providing reagents, Silvia Tacheva and Steeve Boulant for help setting up the experiments with Nup62, and members of our laboratory for helpful discussions.

This work was supported by National Institutes of Health grants GM-075252 (to T. Kirchhausen), U54 AI057159 (New England Regional Center of Excellence in Biodefense and Emerging Infectious Disease, Core Imaging Facility), and SBS SUG M58080013 (to L. Lu).

Submitted: 10 December 2010
Accepted: 11 July 2011

References

Anderson, D.J., and M.W. Hetzer. 2007. Nuclear envelope formation by chromatin-mediated reorganization of the endoplasmic reticulum. *Nat. Cell Biol.* 9:1160–1166. doi:10.1038/ncb1636

Anderson, D.J., and M.W. Hetzer. 2008. Reshaping of the endoplasmic reticulum limits the rate for nuclear envelope formation. *J. Cell Biol.* 182:911–924. doi:10.1083/jcb.200805140

Anderson, D.J., J.D. Vargas, J.P. Hsiao, and M.W. Hetzer. 2009. Recruitment of functionally distinct membrane proteins to chromatin mediates nuclear envelope formation in vivo. *J. Cell Biol.* 186:183–191. doi:10.1083/jcb.200901106

Antonin, W., C. Franz, U. Haselmann, C. Antony, and I.W. Mattaj. 2005. The integral membrane nucleoporin pom121 functionally links nuclear pore complex assembly and nuclear envelope formation. *Mol. Cell.* 17:83–92. doi:10.1016/j.molcel.2004.12.010

Baumann, O., and B. Walz. 2001. Endoplasmic reticulum of animal cells and its organization into structural and functional domains. *Int. Rev. Cytol.* 205:149–214. doi:10.1016/S0074-7696(01)05004-5

Belgareh, N., G. Rabut, S.W. Baï, M. van Overbeek, J. Beaudouin, N. Daigle, O.V. Zatsepina, F. Pasteau, V. Labas, M. Fromont-Racine, et al. 2001. An evolutionarily conserved NPC subcomplex, which redistributes in part to kinetochores in mammalian cells. *J. Cell Biol.* 154:1147–1160. doi:10.1083/jcb.200101081

Bodoor, K., S. Shaikh, D. Salina, W.H. Raharjo, R. Bastos, M. Lohka, and B. Burke. 1999. Sequential recruitment of NPC proteins to the nuclear periphery at the end of mitosis. *J. Cell Sci.* 112:2253–2264.

Burke, B., and J. Ellenberg. 2002. Remodelling the walls of the nucleus. *Nat. Rev. Mol. Cell Biol.* 3:487–497. doi:10.1038/nrm860

Chaudhary, N., and J.C. Courvalin. 1993. Stepwise reassembly of the nuclear envelope at the end of mitosis. *J. Cell Biol.* 122:295–306. doi:10.1083/jcb.122.2.295

Comings, D.E., and T.A. Okada. 1970. Association of chromatin fibers with the annuli of the nuclear membrane. *Exp. Cell Res.* 62:293–302. doi:10.1016/0014-4827(70)90557-4

Crisp, M., and B. Burke. 2008. The nuclear envelope as an integrator of nuclear and cytoplasmic architecture. *FEBS Lett.* 582:2023–2032. doi:10.1016/j.febslet.2008.05.001

Cronshaw, J.M., A.N. Krutchinsky, W. Zhang, B.T. Chait, and M.J. Matunis. 2002. Proteomic analysis of the mammalian nuclear pore complex. *J. Cell Biol.* 158:915–927. doi:10.1083/jcb.200206106

D'Angelo, M.A., D.J. Anderson, E. Richard, and M.W. Hetzer. 2006. Nuclear pores form de novo from both sides of the nuclear envelope. *Science*. 312:440–443. doi:10.1126/science.1124196

Doucet, C.M., J.A. Talamas, and M.W. Hetzer. 2010. Cell cycle-dependent differences in nuclear pore complex assembly in metazoa. *Cell*. 141:1030–1041. doi:10.1016/j.cell.2010.04.036

Drin, G., J.F. Casella, R. Gautier, T. Boehmer, T.U. Schwartz, and B. Antonny. 2007. A general amphipathic alpha-helical motif for sensing membrane curvature. *Nat. Struct. Mol. Biol.* 14:138–146. doi:10.1038/nsmb1194

Dultz, E., and J. Ellenberg. 2010. Live imaging of single nuclear pores reveals unique assembly kinetics and mechanism in interphase. *J. Cell Biol.* 191:15–22. doi:10.1083/jcb.201007076

Dultz, E., E. Zanin, C. Wurzenberger, M. Braun, G. Rabut, L. Sironi, and J. Ellenberg. 2008. Systematic kinetic analysis of mitotic dis- and re-assembly of the nuclear pore in living cells. *J. Cell Biol.* 180:857–865. doi:10.1083/jcb.200707026

Ehrlich, M., W. Boll, A. Van Oijen, R. Hariharan, K. Chandran, M.L. Nibert, and T. Kirchhausen. 2004. Endocytosis by random initiation and stabilization of clathrin-coated pits. *Cell*. 118:591–605. doi:10.1016/j.cell.2004.08.017

Ellenberg, J., E.D. Siggia, J.E. Moreira, C.L. Smith, J.F. Presley, H.J. Worman, and J. Lippincott-Schwartz. 1997. Nuclear membrane dynamics and reassembly in living cells: targeting of an inner nuclear membrane

protein in interphase and mitosis. *J. Cell Biol.* 138:1193–1206. doi:10.1083/jcb.138.6.1193

Ferko, M.C., B.W. Patterson, and P.J. Butler. 2006. High-resolution solid modeling of biological samples imaged with 3D fluorescence microscopy. *Microsc. Res. Tech.* 69:648–655. doi:10.1002/jemt.20332

Franz, C., R. Walczak, S. Yavuz, R. Santarella, M. Gentzel, P. Askjaer, V. Galy, M. Hetzer, I.W. Mattaj, and W. Antonin. 2007. MEL-28/ELYS is required for the recruitment of nucleoporins to chromatin and postmitotic nuclear pore complex assembly. *EMBO Rep.* 8:165–172. doi:10.1038/sj.embor.7400889

Gillespie, P.J., G.A. Khoudoli, G. Stewart, J.R. Swedlow, and J.J. Blow. 2007. ELYS/MEL-28 chromatin association coordinates nuclear pore complex assembly and replication licensing. *Curr. Biol.* 17:1657–1662. doi:10.1016/j.cub.2007.08.041

Goldberg, M.W., C. Wiese, T.D. Allen, and K.L. Wilson. 1997. Dimples, pores, star-rings, and thin rings on growing nuclear envelopes: evidence for structural intermediates in nuclear pore complex assembly. *J. Cell Sci.* 110:409–420.

Haraguchi, T., T. Koujin, T. Hayakawa, T. Kaneda, C. Tsutsumi, N. Imamoto, C. Akazawa, J. Sukegawa, Y. Yoneda, and Y. Hiraoka. 2000. Live fluorescence imaging reveals early recruitment of emerin, LBR, RanBP2, and Nup153 to reforming functional nuclear envelopes. *J. Cell Sci.* 113:779–794.

Haraguchi, T., T. Koujin, M. Segura-Totten, K.K. Lee, Y. Matsuoka, Y. Yoneda, K.L. Wilson, and Y. Hiraoka. 2001. BAF is required for emerin assembly into the reforming nuclear envelope. *J. Cell Sci.* 114:4575–4585.

Haraguchi, T., T. Kojidani, T. Koujin, T. Shimi, H. Osakada, C. Mori, A. Yamamoto, and Y. Hiraoka. 2008. Live cell imaging and electron microscopy reveal dynamic processes of BAF-directed nuclear envelope assembly. *J. Cell Sci.* 121:2540–2554. doi:10.1242/jcs.033597

Harel, A., A.V. Orjalo, T. Vincent, A. Lachish-Zalait, S. Vasu, S. Shah, E. Zimmerman, M. Elbaum, and D.J. Forbes. 2003. Removal of a single pore subcomplex results in vertebrate nuclei devoid of nuclear pores. *Mol. Cell*. 11:853–864. doi:10.1016/S1097-2765(03)00116-3

Hetzer, M.W., T.C. Walther, and I.W. Mattaj. 2005. Pushing the envelope: structure, function, and dynamics of the nuclear periphery. *Annu. Rev. Cell Dev. Biol.* 21:347–380. doi:10.1146/annurev.cellbio.21.090704.151152

Kiseleva, E., S. Rutherford, L.M. Cotter, T.D. Allen, and M.W. Goldberg. 2001. Steps of nuclear pore complex disassembly and reassembly during mitosis in early *Drosophila* embryos. *J. Cell Sci.* 114:3607–3618.

Kremer, J.R., D.N. Mastronarde, and J.R. McIntosh. 1996. Computer visualization of three-dimensional image data using IMOD. *J. Struct. Biol.* 116:71–76. doi:10.1006/jsbi.1996.0013

Lu, L., M.S. Ladinsky, and T. Kirchhausen. 2009. Cisternal organization of the endoplasmic reticulum during mitosis. *Mol. Biol. Cell*. 20:3471–3480. doi:10.1091/mbc.E09-04-0327

Macaulay, C., and D.J. Forbes. 1996. Assembly of the nuclear pore: biochemically distinct steps revealed with NEM, GTP γ S, and BAPTA. *J. Cell Biol.* 132:5–20. doi:10.1083/jcb.132.1.5

Mastronarde, D.N. 1997. Dual-axis tomography: an approach with alignment methods that preserve resolution. *J. Struct. Biol.* 120:343–352. doi:10.1006/jsbi.1997.3919

Mastronarde, D.N. 2005. Automated electron microscope tomography using robust prediction of specimen movements. *J. Struct. Biol.* 152:36–51. doi:10.1016/j.jsb.2005.07.007

Maul, G.G. 1977. Nuclear pore complexes. Elimination and reconstruction during mitosis. *J. Cell Biol.* 74:492–500. doi:10.1083/jcb.74.2.492

Patel, S.S., and M.F. Rexach. 2008. Discovering novel interactions at the nuclear pore complex using bead halo: a rapid method for detecting molecular interactions of high and low affinity at equilibrium. *Mol. Cell. Proteomics*. 7:121–131.

Puhka, M., H. Vihinen, M. Joensuu, and E. Jokitalo. 2007. Endoplasmic reticulum remains continuous and undergoes sheet-to-tubule transformation during cell division in mammalian cells. *J. Cell Biol.* 179:895–909. doi:10.1083/jcb.200705112

Rabut, G., V. Doye, and J. Ellenberg. 2004. Mapping the dynamic organization of the nuclear pore complex inside single living cells. *Nat. Cell Biol.* 6:1114–1121. doi:10.1038/ncb1184

Rasala, B.A., A.V. Orjalo, Z. Shen, S. Briggs, and D.J. Forbes. 2006. ELYS is a dual nucleoporin/kinetochore protein required for nuclear pore assembly and proper cell division. *Proc. Natl. Acad. Sci. USA*. 103:17801–17806. doi:10.1073/pnas.0608484103

Rasala, B.A., C. Ramos, A. Harel, and D.J. Forbes. 2008. Capture of AT-rich chromatin by ELYS recruits POM121 and NDC1 to initiate nuclear pore assembly. *Mol. Biol. Cell*. 19:3982–3996. doi:10.1091/mbc.E08-01-0012

Rotem, A., R. Gruber, H. Shorer, L. Shaulov, E. Klein, and A. Harel. 2009. Importin beta regulates the seeding of chromatin with initiation sites for nuclear pore assembly. *Mol. Biol. Cell*. 20:4031–4042. doi:10.1091/mbc.E09-02-0150

Sheehan, M.A., A.D. Mills, A.M. Sleeman, R.A. Laskey, and J.J. Blow. 1988. Steps in the assembly of replication-competent nuclei in a cell-free system from *Xenopus* eggs. *J. Cell Biol.* 106:1–12. doi:10.1083/jcb.106.1.1

Voeltz, G.K., W.A. Prinz, Y. Shibata, J.M. Rist, and T.A. Rapoport. 2006. A class of membrane proteins shaping the tubular endoplasmic reticulum. *Cell*. 124:573–586. doi:10.1016/j.cell.2005.11.047

Walther, T.C., A. Alves, H. Pickersgill, I. Loïodice, M. Hetzer, V. Galy, B.B. Hülsmann, T. Köcher, M. Wilm, T. Allen, et al. 2003. The conserved Nup107-160 complex is critical for nuclear pore complex assembly. *Cell*. 113:195–206. doi:10.1016/S0092-8674(03)00235-6

Yang, L., T. Guan, and L. Gerace. 1997. Integral membrane proteins of the nuclear envelope are dispersed throughout the endoplasmic reticulum during mitosis. *J. Cell Biol.* 137:1199–1210. doi:10.1083/jcb.137.6.1199

Zuccolo, M., A. Alves, V. Galy, S. Bolhy, E. Formstecher, V. Racine, J.B. Sibarita, T. Fukagawa, R. Shiekhattar, T. Yen, and V. Doye. 2007. The human Nup107-160 nuclear pore subcomplex contributes to proper kinetochore functions. *EMBO J.* 26:1853–1864. doi:10.1038/sj.emboj.7601642